# The Structure of the Auto-Ignition Region of Turbulent Dilute Methanol Sprays Issuing in a Vitiated Co-flow

**William O'Loughlin · Assaad R. Masri**

**Abstract** This paper presents planar imaging of laser induced fluorescence (LIF) from key reactive species in the auto-ignition region of dilute turbulent spray flames of methanol. High-speed (5 kHz) LIF-OH imaging as well as low speed (10 Hz) imaging of joint LIF-OH-$CH_2O$ is performed. The product of the OH and $CH_2O$ signals is used as a qualitative indicator of local heat release. The burner is kept intentionally simple to facilitate computations and the spray is formed upstream of the jet exit plane and carried with air or nitrogen into a hot co-flowing stream of vitiated combustion products. The studied flames are all lifted but differ in the shape of their leading edge and heat release zones. Similarities with auto-ignition of gaseous fuels, as well as differences, are noted here. Formaldehyde is detected earlier than OH implying that the former is a key precursor in the initiation of auto-ignition. Growing kernels of OH that are advected from upstream, close in on the jet centreline and ignite the main flame. The existence of double reaction zones in some flames may be due to ignitable mixtures formed subsequent to local evaporation of droplets and subsequent mixing. When air is used as spray carrier, reaction zones broaden with distance, possibly due to increased partial premixing and regions of intense heat release occur near the flame centreline further downstream. With nitrogen as carrier, the flame maintains a nominal diffusion-like structure with reaction zones of uniform width and substantially less concentration of heat release on the flame centreline.

**Keywords** Turbulent flames · Auto-ignition · Dilute sprays · Partially premixed flames · LIF imaging

W. O'Loughlin (✉) · A. R. Masri
School of Aerospace, Mechanical and Mechatronic Engineering,
The University of Sydney, Sydney, NSW, 2006 Australia
e-mail: william.oloughlin@sydney.edu.au

# 1 Introduction

A novel burner aimed at studying the auto-ignition of turbulent, dilute spray jets issuing in a hot vitiated co-flow was introduced in an earlier paper where a range of liquid fuels were studied [1]. The burner design is kept intentionally simple to facilitate modeling such that the spray is formed upstream and carried to the jet exit plane with either air or nitrogen. The key controlling parameters were found to be the temperature of the hot co-flowing stream, the spray loading to gas carrier ratio, and the bulk velocity of the carrier fluid. The flames stabilized are visibly lifted showing a region closer to the jet exit where heat release is evolving and the flame is barely visible; and a more intense flaming region further downstream. The flames were characterized with respect to their lift-off heights and a relevant controlling parameter. A range of cases is selected for further investigations with a focus on methanol fueled flames. Qualitative, high-speed (5 kHz) imaging of LIF-OH and chemi-luminescence from CH* along with detailed measurements of the flow fields, droplet fluxes and mean temperature fields have shown that auto-ignition is complicated by the surrounding droplets in ways that are not well understood. The objective of this paper is to shed more light on this process.

The hot vitiated co-flow burner has provided an excellent medium for studying auto-ignition in gaseous flows [2, 3]. Cabra et al. have performed some preliminary work of auto-ignition in methanol spray flames using the vitiated co-flow burner [4, 5]. Another extremely useful configuration that serves a similar purpose uses preheated air to initiate combustion [6]. A significant body of knowledge is now available on the auto-ignition of selected gaseous fuels. Earlier investigations of methane issuing in hot vitiated co-flows, revealed the existence of "kernels" that develop at some distance downstream of the jet exit plane and travel further downstream to initiate flaming combustion [2]. This scenario for the auto-ignition of gaseous flames has been confirmed by both large eddy simulations (LES) [7] as well as direct numerical simulations (DNS) [8–12] which also indicate that the dominant radicals in these kernels are $CH_2O$ in methane fuels and $HO_2$ in hydrogen fuels. These DNS studies also reinforced the concept of ignition being initiated at the most reactive mixture fraction, $\xi_{MR}$ [9, 13]. In the case of stratified hydrogen-air fuels [14, 15] ignition kernels were found to initiate (at $\xi_{MR}$) in lean mixtures that have relatively low scalar dissipation rates before propagating into stoichiometric and richer mixtures.

The relevant question here is how does the presence of droplets affect auto-ignition and how different is this process from that discussed above for the gas phase? More specifically, the existence, or otherwise, of kernels that initiate flaming combustion, the evolution of heat release in the early part of the flow, and the mixtures that are most susceptible to auto-ignition are key issues that need to be addressed for dilute sprays. While there are extensive experimental data reporting ignition delays of sprays [16, 17], detailed information about the nature of locally evolving compositional structures are scarce due to the difficulty of applying advanced laser diagnostics to spray flows. To date, computations of auto-igniting sprays are further advanced than experiments with approaches such as particle-based probability density functions [18, 19], large eddy simulations [20, 21], and conditional moment closure (CMC) methods [22–24] revealing differences but also similarities between the auto-ignition of gaseous and liquid fuels. Similarly, detailed 3D-DNS

studies of auto-igniting sprays are now starting to emerge with increasing levels of complexity [25–27]. The initial findings confirm earlier calculations using CMC [13] and indicate that the onset of auto-ignition is delayed with increasing droplet size but the mixtures that are most reactive are indeed similar to those obtained for the gas phase and do not seem to depend on the size of droplets.

This paper extends earlier experimental investigations of the auto-ignition of dilute sprays [1] by presenting additional measurements in selected flows of methanol fuels. Joint laser induced fluorescence imaging of OH and $CH_2O$ (LIF-OH-$CH_2O$) performed at a repetition rate of 10 Hz (referred to heron as low-speed), as well as high-speed (5 kHz) imaging of LIF-OH, albeit qualitative, reveal novel information about the evolving structure of the reaction zones and the pockets of heat release. The product $[OH]x[CH_2O]$ has been used earlier as an adequate marker of heat release not only in gaseous diffusion and premixed flames [28–30] but in reacting sprays as well [31]. Recently, and using the vitiated co-flow burner developed by Dally et al. [32] for studying MILD combustion under reduced and variable levels of oxygen, Medwell et al. [33, 34] reported imaging of LIF-OH-$CH_2O$ in ethylene flames. The product of $[OH][CH_2O]$ measured in regions upstream of the visible base of these ethylene flames indicate the presence of some heat release associated with the auto-ignition region. The intensity of this heat release increases as the visible part of the flame is approached. These issues will also be addressed here for turbulent auto-igniting flames containing droplets.

## 2 Experimental

This section provides a brief outline of the burner, the stability limits and the flames selected for further study. It then describes the experimental approaches with respect to the low-speed and high-speed LIF imaging; and concludes by providing a justification for using the product of the LIF signals from OH and $CH_2O$ as a qualitative measure of heat release.

### 2.1 Stability limits and selected flames

A cutaway view of the burner is shown in Fig. 1. A basic feature of the design is to maintain simplicity and overall similarity to earlier studies of gaseous auto-ignition in vitiated co-flows [2]. This necessitates that the spray be formed upstream of the exit plane of the jet using an ultrasonic generator (Sonotek) that produces droplets with a Sauter mean diameter of around 40 μm. The spray is carried by a co-flowing stream of air (or nitrogen, as specified) at room temperature through the central fuel pipe that is 196 mm long, has an inner diameter of 4.6 mm and a wall thickness of 0.8 mm which has been tapered down to 0.25 mm at the exit plane. The outer co-flow is 197 mm in diameter bringing hot vitiated products from about 2200 premixed hydrogen/air flames issuing from 1.58 mm diameter holes on a perforated plate situated 68 mm upstream of the exit plane of the central spray pipe. The co-flow composition is assumed to be the equilibrium products of a hydrogen/air flame which at the equivalence ratio required to give 1430K is $N_2$ 0.73, $H_2O$ 0.15, $O_2$ 0.12 by volume with small amounts of $H_2$, OH, H and O. The co-flow velocity has not been

**Fig. 1** Schematic of the burner
showing important features.
The inset shows the details of
the nebulizer coupling with the
entrance to the central jet
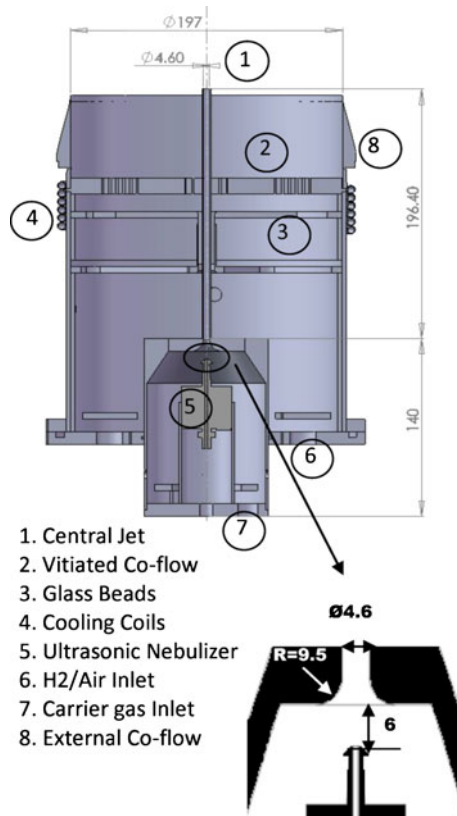


1. Central Jet
2. Vitiated Co-flow
3. Glass Beads
4. Cooling Coils
5. Ultrasonic Nebulizer
6. H2/Air Inlet
7. Carrier gas Inlet
8. External Co-flow

measured, however by calculation from the flow rates and temperature it is expected
to be 3.5 m/s.

It was reported earlier [1] that the key parameters controlling the auto-ignition
and stability characteristics of this burner are (i) the temperature of the hot co-flow
($T_c$), (ii) the bulk jet velocity of the spray carrier ($U_{jc}$), and (iii) the mass ratio of
fuel over gas carrier in the central jet ($M_f/M_c$) (also referred to as "fuel loading").
The focus of this paper is on methanol fuel with air or nitrogen used as carrier. Two
plots of the lift-off heights for methanol flames are shown in Fig. 2 for air carrier
velocity of $U_{jc} = 75$ m/s; one versus co-flow temperature, $T_c$, for fixed values of
fuel loading, $M_f/M_c$, and the other versus fuel loading, $M_f/M_c$ for fixed values of
co-flow temperature, $T_c$. The lift-off height is defined here as the mean location of
the flame base where light blue emissions are detected on still images taken with a
normal digital camera and at an f#3.3 with 0.25 sec exposure. An average of three
images are used for each measurement of the lift-off height, $L_h$ which is normalised
here by the jet diameter (D = 4.6 mm). The horizontal dashed line on each plot
represents the end of the region where the flame is shrouded by the hot co-flow. This
is referred to as the 'valid cone' within which all subsequent measurements are made.
Further downstream of the 'valid cone', the jet fluid becomes gradually exposed to
the laboratory air.

**Fig. 2** Plots of lift-off height ($L_h$) for methanol, normalized by fuel jet diameter (D) and plotted for a fixed carrier velocity ($U_j$) (**a**) verses fuel loading ($M_f/M_c$) for various co-flow temperatures ($T_c$) and (**b**) verses co-flow temperature ($T_c$) for a range of fuel loadings ($M_f/M_c$). The *dashed line* indicates the limit of the valid hot cone of the co-flow and the circles on the 1430K profile indicate flames Mt2A, Mt2B and Mt2C (*left* to *right*). The circle on the 1380K profile indicates the flame on which the high speed data is collected
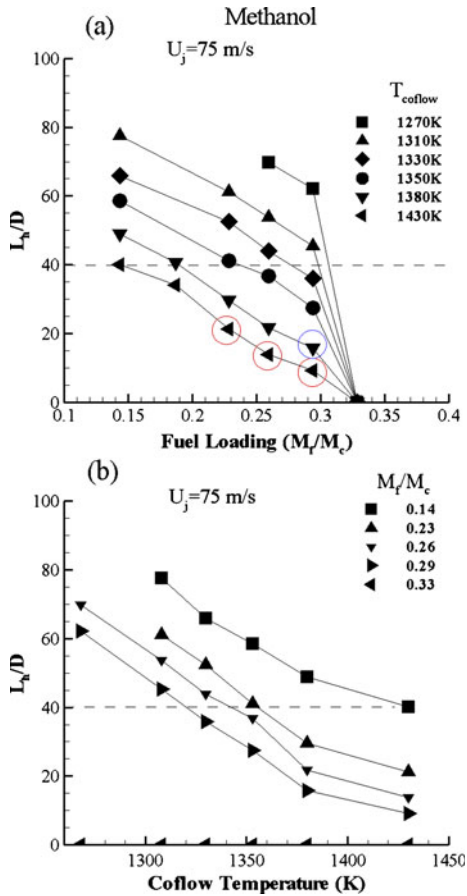


Seven flames are selected for further investigations and relevant parameters for each of these cases are shown in Table 1. Four flames use air as spray carrier while the remaining three use nitrogen carrier, and all cases have a bulk carrier velocity $U_{jc} = 75$ m/s. Flames Mt2A, Mt2B and Mt2C use air as carrier and are shown by circles in Fig. 2a while flames Mt2AN Mt2BN and Mt2CN, with nitrogen carrier are not shown but are found to have lift-off heights similar to their air equivalents. It should be noted that labels A, B and C refer to the type of flames observed when using air as carrier. Type A flames show a distinct cone structure just downstream of the initial ignition region whereas in a type C flame the fuel jet has penetrated the centre of the cone and formed a more annular structure at its base. Type B flame is part way between the other two types A and C. The transition from the cone-like base in flame Mt2A to the annular base in flame Mt2C is clearly illustrated in the visual images of these flames shown on the top row of Fig. 3. Also shown in the bottom row of Fig. 3 are visual images for flames Mt2AN, Mt2BN and Mt2CN. It is evident that using nitrogen as carrier does not result in the conical, luminous base and all flames have an annular like structure. Despite this, the labels A, B and C are maintained here for convenience even for the flames using nitrogen as carrier since

**Table 1** Important parameters for the methanol flames investigated here

| Carrier | Mt2A Air | Mt2AN Nitrogen | Mt2B Air | Mt2BN Nitrogen | Mt2C Air | Mt2CN Nitrogen | Mt1C Air |
|---|---|---|---|---|---|---|---|
| Co-flow temperature (K) | 1430 | 1430 | 1430 | 1430 | 1430 | 1430 | 1380 |
| Bulk jet carrier velocity (m/s) | 75 | 75 | 75 | 75 | 75 | 75 | 75 |
| Jet Reynolds number | 23750 | 23400 | 23750 | 23400 | 23750 | 23400 | 23750 |
| Mass flow rate of carrier gas (g/min) | 91.6 | 88.6 | 91.6 | 88.6 | 91.6 | 88.6 | 91.6 |
| Mass flow liquid fuel (g/min) | 20.4 | 20.4 | 23.8 | 23.8 | 27.1 | 27.1 | 27.1 |
| Fuel loading, $M_f/M_c$ | 0.225 | 0.23 | 0.26 | 0.27 | 0.295 | 0.305 | 0.295 |
| Percentage fuel vapor[a,d] (by mass) | 1.8% | | 4.7% | | 8.0% | | 7.9% |
| Jet equivalence ratio[b,d] (vapor only) | 0.11 | | 0.29 | | 0.50 | | 0.49 |
| Overall jet equivalence ratio[c,d] | 1.39 | | 1.62 | | 1.85 | | 1.85 |
| Measured centerline exit plane temperature (K) | 283 | | 287 | | 288 | | |

[a]Calculated from the volume flux measurements collected on the PDA system
[b]Calculated using the fuel vapor and carrier air only
[c]Calculated using all fuel (liquid and vapor) and carrier air
[d]At the jet exit plane

these cases also have an increasing mass loading of spray and have equivalent flow conditions to their air-carrier counterparts.

Table 1 also shows that, at the jet exit plane of flames Mt2A, Mt2B and Mt2C, the percentage of fuel vapor increases from 1.8% to 8% by mass such that the equivalence ratio in the gas phase increases from 0.11 to 0.5 confirming that the gaseous fuel mixtures exiting the jet are still lean, on average. The overall equivalence ratio which accounts for the entire supply of fuel and air is also presented in Table 1 for the jet exit plane condition of flames Mt2A, Mt2B and Mt2C. These three parameters are not relevant for the flames using nitrogen as carrier and hence not shown. The exit plane centerline mean temperature is also reported for flames Mt2A, Mt2B and Mt2C measured using a K-type thermocouple. The decrease below ambient temperature is due to evaporation of the fuel. The temperatures were not measured for the other flames since their liquid fuel flow rates are the same as the three measured cases.

### 2.2 Experimental methods

Mean temperature profiles are measured using a thermocouple inserted in methanol flames Mt2A, Mt2B and Mt2C. This is justified given that established laser-based temperature measurement techniques, such as Rayleigh scattering, cannot be applied here. A platinum-rhodium thermocouple is used (Pt-5%Rh with Pt-20%Rh) with a bead diameter of ~0.2 mm. Radial profiles of temperature are taken at various axial locations ranging from $x/D = 5$ to $x/D = 40$. At the exit plane, temperatures near the jet centerline are close to room temperature and therefore a standard K-type thermocouple was used at this location. Fluctuations in the measured temperature may be higher here than in turbulent gaseous flows, possibly as a result of droplets
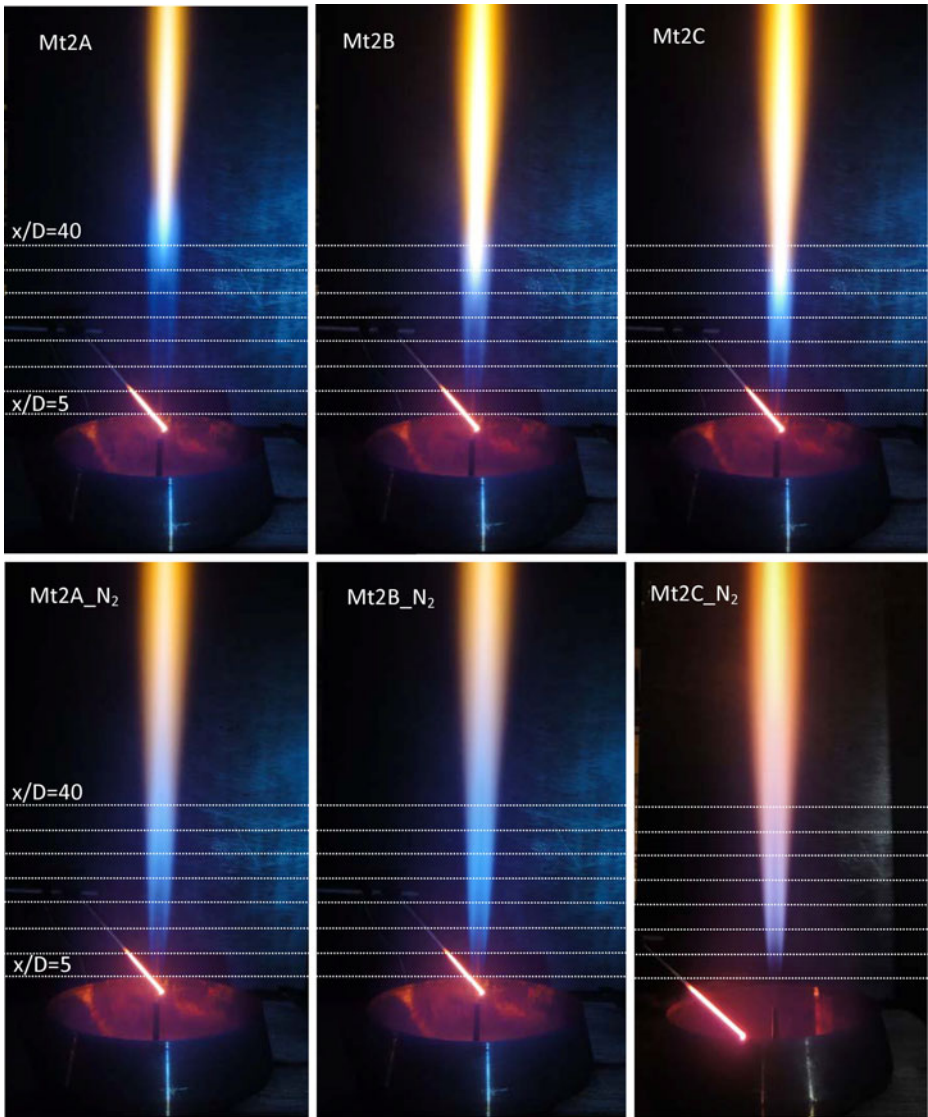
**Fig. 3** Digital camera images of the six flames of interest. The *dashed white lines* show the axial locations in the flames starting at x/D = 5 increasing in 5 D increments up to x/D = 40

impacting on the thermocouple bead. To illustrate this, 100 samples are taken at each measurement location and the extent of the fluctuation is reflected by the error bars showing one standard deviation around each mean value plotted in Fig. 8. All temperature measurements reported here are not corrected for radiation. While it is realized that radiation will be important at certain locations, the overall trend would not be affected.

### 2.2.1 Low-speed LIF-OH-CH₂O system

Joint LIF imaging of OH and $CH_2O$ is performed at a repetition rate of 10 Hz and this is referred to hereon as low-speed LIF-OH-$CH_2O$ imaging. Although the measurements are qualitative, the joint product of [OH][$CH_2O$] provides a reasonable marker of the regions of heat release [26–29]. A schematic of the experimental set-up is shown in Fig. 4. Excitation of the OH radical utilized the Q1(6) line at 283.01 nm produced using an Nd:YAG pumped (Sirah) dye laser containing Rhodamine 6G dye dissolved in ethanol. The dye laser is tuned to produce radiation at 566.02 nm which is subsequently frequency doubled in a BBO crystal to produce the desired wavelength. Measurements were conducted using a maximum UV output of about 10 mJ per pulse at 10 Hz. Even though significantly higher energies could have been achieved, the occurrence of laser induced droplet breakdown necessitated such a lower threshold.

Laser induced fluorescence of formaldehyde ($CH_2O$) is performed using an excitation line at 353.17 nm which is obtained using another Nd:YAG pumped (Sirah) dye laser. The frequency doubled output from the Nd:YAG is used to pump Pyridine 1 (LDS 698) dye dissolved in ethanol which is tuned to an output at 706.34 nm. This output is then frequency doubled in a KDP crystal to produce the desired output. The maximum power that could be obtained at the UV wavelength was 20 mJ per pulse. However, this had to be detuned to 14 mJ per pulse due to laser-induced droplet breakdown.

Sheet-forming optics is used to produce plane thicknesses of about 200 microns for both OH and $CH_2O$ laser beams. A 1000 mm focal length lens (RCX-40.0-30.0-508.6 UV, CVI product) is used to focus the beams and a 400 mm focal length lens (RCC-40.0-30.0-203.2-UV, CVI product) is used to expand the beams to a sheet with height
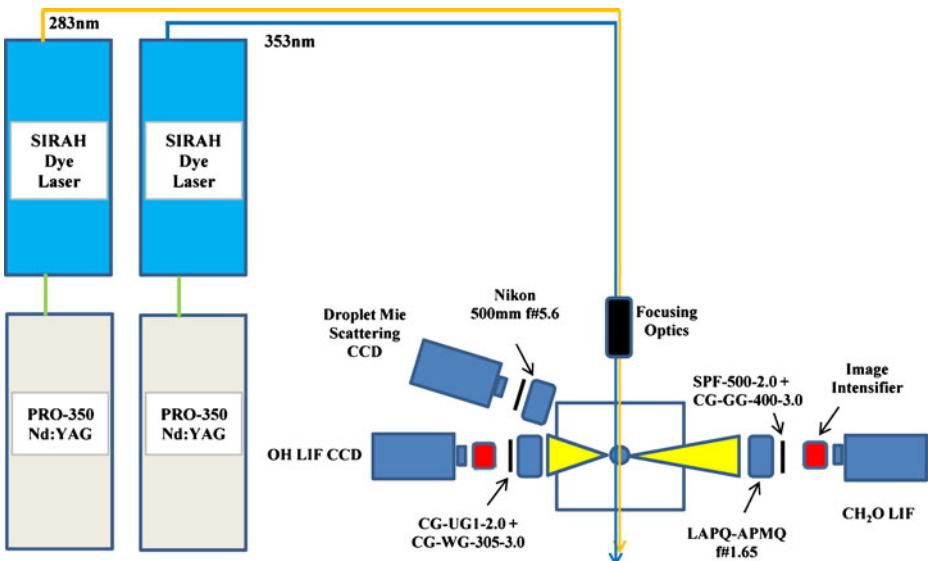


**Fig. 4** Schematic of the low speed (10 Hz) experimental set-up

of 15 mm. The long focal length of the focusing lens was required to help prevent laser induced droplet breakdown from occurring.

Collection of the OH signal is done using an image intensifier coupled to a CCD camera. The intensifier is a single-stage system operated with a gate width of 2 μs. The LIF signal is focused using an f#1.65 LAPQ/APMQ (CVI product) UV lens with a clear aperture of 60 mm. The intensifier output is coupled to the camera using an f#1.2 Nikkor 50 mm lens. Filtering of the signal is achieved using a 2 mm thick UG-1 filter (CG-UG-1-2.0, CVI product) together with a 3 mm thick long pass WG-305 filter (CG-WG-305-3, CVI product). This combination of filters provided a blocking OD of 10 at the laser wavelength while allowing transmission of 7.3% at the collection wavelength of 310 nm. The severity of the filtering was required in order to reduce the interfering signal from the droplets to a level that would be safe for the intensifier. The strength of the LIF-OH meant that good signal to noise ratios are achieved despite the low signal transmission.

Collection of the $CH_2O$ signal used an identical setup to the OH system described above with the exception of the filtering. A combination of a short-wave pass (SPF-500-2.0, CVI product) and long-wave pass (CG-GG-400-3.0, CVI product) filter is used to isolate the LIF signal (between 400 and 500 nm) from the elastic scattering at the laser wavelength at 353.17 nm. The chip size of the CCD cameras is $688 \times 520$ pixels and the image size at the measurement location in real space is $25 \times 19.7$ mm giving a spatial resolution of 0.036 mm/pixel. Noise reduction in the $CH_2O$ images is performed in post-processing using a $6 \times 6$ gaussian filter. No noise removal in the post-processing of the OH images is performed. The peak signal to noise ratio of the images is approximately 15 for the $CH_2O$ images after filtering and 10 for the OH images at the furthest downstream location however this decreases for images closer to the jet exit plane.

### 2.2.2 High-speed LIF-OH system

High speed LIF-OH is performed at a repetition rate of 5 kHz. Excitation of the OH radical occurs at the same wavelength as the low speed LIF-OH and is generated using a Nd-YAG (Edgewave, IS4II-E) pumped dye laser (Sirah) containing Rhodamine 6G dye. The diode pumped Nd:YAG laser produces about 12 W of radiation at 532 nm with a repetition rate of 5 kHz. The fundamental beam from the dye is frequency doubled to produce about 0.15 mJ/pulse of laser energy at the desired wavelength of 283.01 nm.

Signal collection is performed on a CMOS camera (LaVision High Speed Star 6) coupled with a dual-stage intensifier (La Vision High Speed IRO). The collected light is focused using two sets of LAPQ/APMQ three-element lenses with a clear aperture of 60 mm (f#1.65). The camera has an array of $1024 \times 1024$ pixels and the intensifier gate is set at 200 ns. The signal is filtered using a 3 mm thick long pass 295 nm filter, a 3 mm thick long pass 305 nm filter and a 1 mm UG11 filter (CG-WG-295-2x2-3, CG-WG-305-2x2-1, CG-UG-11-1.0, CVI products). This level of filtering was necessary to completely remove the stray signal emitted from droplets. The entire system is run at a repetition rate of 5 kHz, thus producing a time interval of 200 μs between subsequent images. The camera has a chip size of $1024 \times 1024$ pixels and the image size at the measurement location in real space is $58 \times 58$ mm which gives a spatial resolution of 0.057 mm/pixel. The peak signal to noise ratio of the images

is approximately 10 at the furthest downstream location and decreases for images closer to the exit plane.

2.3 Indicator of heat release

As discussed earlier, the product of [CH₂O][OH] has been used as a convenient and somewhat reliable marker of heat release in both turbulent gaseous flames [29, 35] as well as in turbulent dilute spray flames [31]. The same approach is adopted to provide a qualitative marker of heat release zones in the auto-igniting flames studied here. It is well known that LIF-CH₂O suffers from interferences that arise mainly in rich mixtures due to the existence of heavier hydrocarbons and soot precursors. Considering that heat release zones lie generally around stoichiometric or slightly
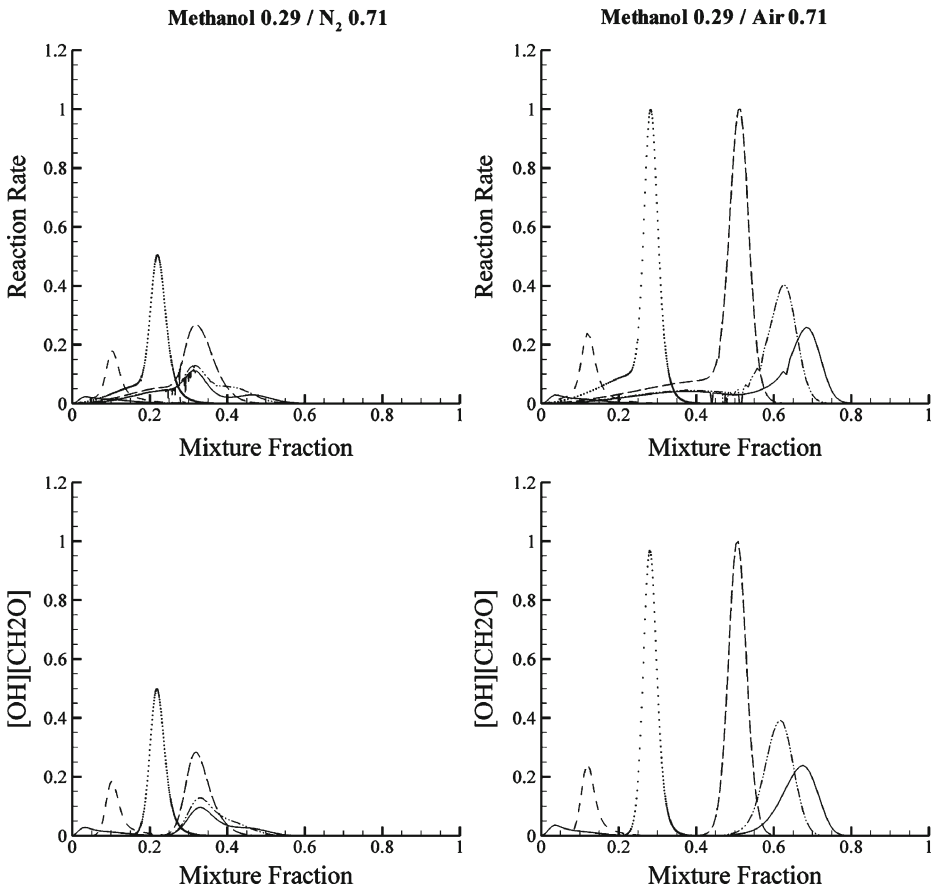


**Fig. 5** Zero Dimensional Conditional Moment Closure calculations of the auto-ignition of a methanol/air mixture (*left*) and a methanol/nitrogen mixture (*right*). The top graphs show the reaction rate as a function of mixture fraction at a series of equally spaced time intervals during the ignition process. The bottom uses the same positions in time but shows the product [OH][CH₂O]

rich mixtures, it has been demonstrated earlier [31] that such interference has little effect on the product of [CH$_2$O][OH] which remains a good marker of heat release.

The validity of such an indicator in transient auto-igniting flames is now demonstrated using calculations of unsteady, zero dimensional auto-ignition of methanol using a CMC code developed at the University of Cambridge [24, 36]. A reduced chemical kinetic mechanism consisting of 32 species and 167 reactions is used which is based on the detailed mechanism reported by Lindstedt et al. [37]. The left and right boundary conditions are fixed and the reaction proceeds in mixture fraction space. In this case, the left boundary condition is set to be the conditions of the co-flow, which is 1430 K with a composition of the combustion products of a hydrogen air flame at the appropriate equivalence ratio. The right boundary condition is set to 0.29 by mass of methanol with the balance made up of nitrogen or air. A prescribed bell-shaped distribution of the scalar dissipation in mixture fraction space is used and the peak value of the scalar dissipation is set to 50 s$^{-1}$. Figure 5 (left) shows the reaction rate and product [OH][CH$_2$O] for a methanol/nitrogen mixture and Fig. 5 (right) shows the same for a methanol/air mixture. The reaction rate data is normalized by the peak reaction rate of both cases so that a relative comparison can be made between the air and nitrogen carriers. Likewise, the [OH][CH$_2$O] data is normalized by the peak value of [OH][CH$_2$O] obtained from either case. The location and width of the peaks of reaction rate correlate very well with those for the product [OH][CH$_2$O]. The only real difference is in the 'tail' that extends out to the lean side of the reaction rate peaks. Considering that these 'tails' are only about 10% the height of the peak value it can be considered that the heat release in these regions is small compared to the main heat release and so the product [OH][CH$_2$O] is still a good marker of the main heat release zones. Furthermore, dilution with either nitrogen or air is shown not to affect the validity of this assumption.

## 3 Results

A sample of images is presented here for both the low-speed measurements of LIF-OH and LIF-CH$_2$O as well as the high-speed images of OH. The images are qualitative and not corrected for quenching so processing is limited to background subtraction, beam profile correction and the application of smoothing filters to reduce noise. The images shown are selected to be as representative as possible of the entire data set which is huge but may be made available on request.

### 3.1 Low-speed LIF-OH-CH$_2$O images

Figure 5 shows representative images of LIF-OH and LIF-CH$_2$O as well as their product, (labeled HR$_I$) as a qualitative indicator of heat release zones. Images are shown for nine axial locations covering the domain of x/D = 0 to 40 in each of flames Mt2B, Mt2C, Mt2BN and Mt2CN. Each individual image covers a height of 19.7 mm (about 4.3 jet diameters) and a width of 26 mm. These measurement locations are highlighted on Fig. 3 with respect to the visible appearance on each flame and are all within the "valid cone" where the fuel stream is believed to be interacting with gases originating from the hot co-flow but not from the laboratory air. It should be noted that the images stacked here at successive axial locations are not continuous,

neither in space nor in time and are shown here for illustration only. The following observations are made:

- Near the exit plane, formaldehyde formation occurs earlier than OH as is clear from the first two rows of images at x/D = 0 and 5 where OH is never detected at x/D = 0 while pockets of formaldehyde may occur there as can be seen for the image of flame Mt2BN. At x/D = 10, pockets of OH occur more frequently although in some cases the OH profiles are seen to be continuous and more representative of a connected reaction zone. The existence of flame kernels in the initiation region of auto-ignition is further discussed later with respect to the high-speed images of OH.

- The pockets of OH become more connected with downstream distance implying the establishment of continuous reaction zones which start at outer radial locations and gradually approach the centerline at x/D = 30 to 40. Images of formaldehyde show broad profiles that extend toward the centerline even at x/D = 5 or 10. It should be noted that as fuel-rich regions are approached, the measured formaldehyde is subject to stronger interferences from heavier hydrocarbon molecules so that the $CH_2O$ signals detected closer to the centerline may be largely artificial.

- Further downstream, increased wrinkling of the formaldehyde is seen to occur until approximately x/D = 35. At x/D = 40, the formaldehyde becomes patchy with some images showing no or very little signal from $CH_2O$ as can be seen for flame Mt2C. This is consistent with the fact that at these downstream locations the ignition process is complete, the flame is well established, significant premixing has occurred and the fuel is gradually consumed.

- Pockets of heat release, $HR_I$ as revealed by images of the product $[OH][CH_2O]$, start to appear at x/D = 10 to 15 and these become gradually more connected further downstream with the reaction zones becoming more wrinkled as they approach the centerline at x/D > 30. Double reaction zones are observed in approximately 10–20% of the images and examples of a double reaction zone may be seen at x/D = 40 in flame Mt2B as well as at x/D = 25 − 30 in flame Mt2C.

- Zones of heat release are normally very thin as they form at upstream locations. Further downstream, the reaction zones of flames Mt2B and Mt2C which use air as spray carrier become broader while those of flames Mt2BN and Mt2CN remain relatively thin. This is consistent since the latter flames use nitrogen as spray carrier and hence are more likely to maintain a diffusion-like flame structure.

- Another difference between the flames that use air or nitrogen as carrier lies in the measured intensity of the OH signal. At a given axial location, the signal strength of OH in flames Mt2BN and Mt2CN is lower than in flames Mt2B and Mt2C. In contrast, the intensity in the formaldehyde signal is somewhat similar in all flames.

3.2 High-speed LIF-OH images

Figure 7 shows two sequences of high speed images of LIF-OH measured at four axial locations in methanol flame Mt1C. This case has a bulk air carrier jet velocity of 75 m/s and a co-flow temperature of 1380K which is slightly lower than that used

for the Mt2 flames (see Table 1 for details). Flame Mt1C has a lift-off height of around 15.7 diameters as is seen from the plots presented in Fig. 2. Each LIF-OH image covers a region of 58 mm × 50 mm and sequences of images are shown for axial locations ranging from x/D = 2 to 42 in intervals of 10 diameters per row as indicated on the figure. The images are sequenced in time from left to right with a time interval of 200 μs between successive images while the images shown for different axial locations are not sequenced neither in space nor in time. Moving from left to right on each row of images shows the evolution of LIF-OH at that particular axial location. The complete data set contains thousands of similar time-sequences. The following observations are made:

- Consistent with the images reported in Fig. 6, there is no presence of OH close to the jet exit plane and the first kernels of OH start to appear and grow in the next row of images as indicated by the arrows which also show the growth of these kernels with time. Given a time separation of 200microseconds between images, it is estimated that these kernels are advected at a speed of about 15 m/s. The growth rate in the surface area (or volume) of these kernel varies significantly as illustrated in the two sequences shown here since this depends on the local condition in the proximity of the kernel.
- The third row of images which correspond to x/D = 22 − 32 shows that at this location, breakages occur in an otherwise continuous string of LIF-OH implying the existence of local extinction (see lower sequence of Fig. 7). In the third row of the upper sequence, closure of an existing breakage occurs. Such "breakages" and "closures" are consistent with earlier findings recently reported in pilot-stabilized turbulent non-premixed gaseous flames [38].
- At x/D = 32 − 42, and consistent with the images shown in Fig. 6, the intensity of the measured LIF-OH signals increase significantly. Moreover, the OH profiles remain highly distorted but become broader and converge gradually on the centerline. This corresponds to the region where the flame becomes luminous with an intense blue region on the centerline (not shown).

3.3 Flow, droplets fluxes and temperature fields

Figure 8 shows radial profiles of velocity, turbulence, liquid flux and mean temperature measured at x/D = 0.4, 10, 20 and 30 in flame Mt2B. The top four rows show, radial profiles of the mean axial and radial velocities, $\bar{u}$ and $\bar{v}$ and their rms fluctuations, $u'$ and $v'$, respectively. The fifth row shows the liquid volume flux and the bottom row shows the mean temperature profiles. In each plot shown in the top five rows, the radial profiles are presented for the unconditional results referred to as "All Sizes", as well as for measurements conditioned with respect to five specific bands of droplet size in increasing order d < 10, 10 < d < 20, 20 < d < 30, 30 < d < 40 and 40 < d < 50 μm. In some cases, the smallest size bin (0 < d < 10 μm) is omitted due to lack of data in the bin. Droplets with diameters less than 10 μm are deemed to correspond to the gas phase velocity. It should be noted that the LDV/PDA signal measured here use droplets as the scattering medium and there is no additional seeding of particles in the co-flowing air stream. This is why the radial profiles are truncated at radial locations limited to regions where sufficient amounts of droplets are present. The bias introduced in the measurement due to lack
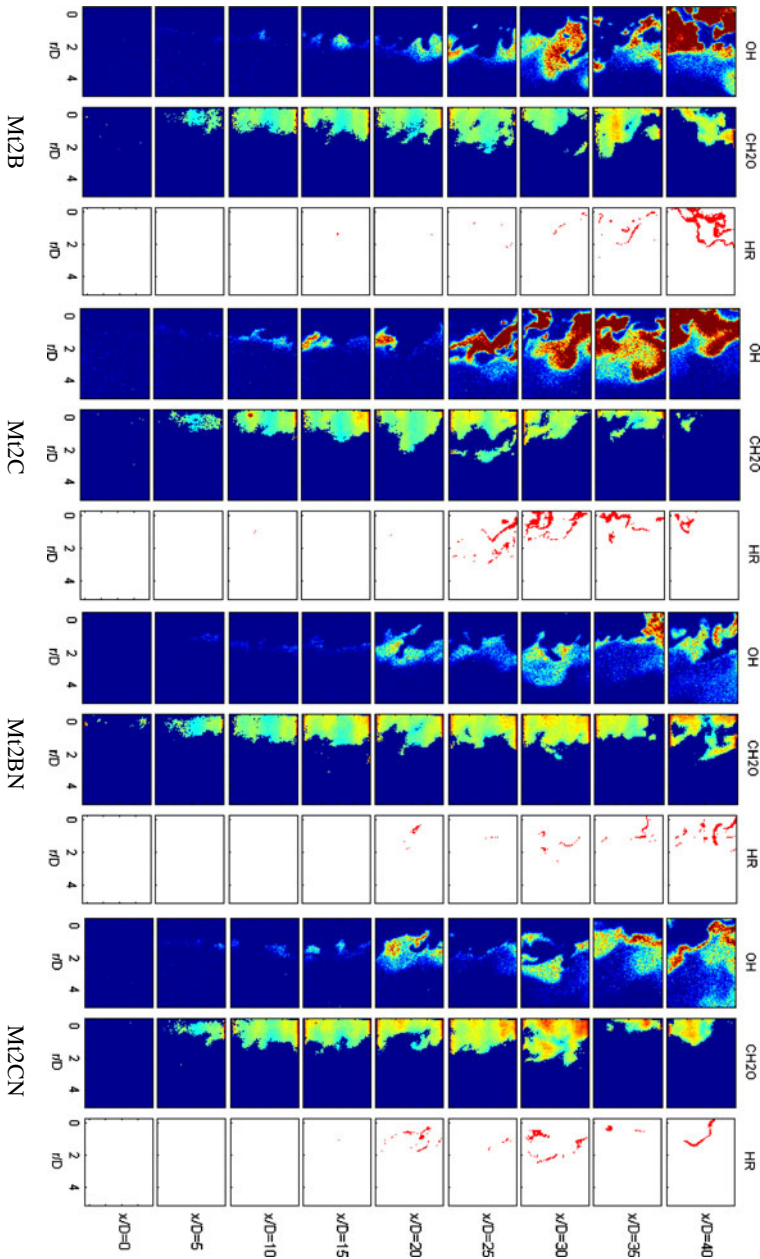
**Fig. 6** Low Speed (10 Hz) joint imaging of OH and $CH_2O$ in two methanol flames. The column marked $HR_I$ is the product of the OH and $CH_2O$ images which is used as an indicator of heat release. Each individual image has dimensions of 26 mm × 19.7 mm

of seeding is only significant only at the outer boundaries of the jet and is estimated to peak at about 6% and 15%, respectively, for the mean axial velocity and its rms fluctuations.
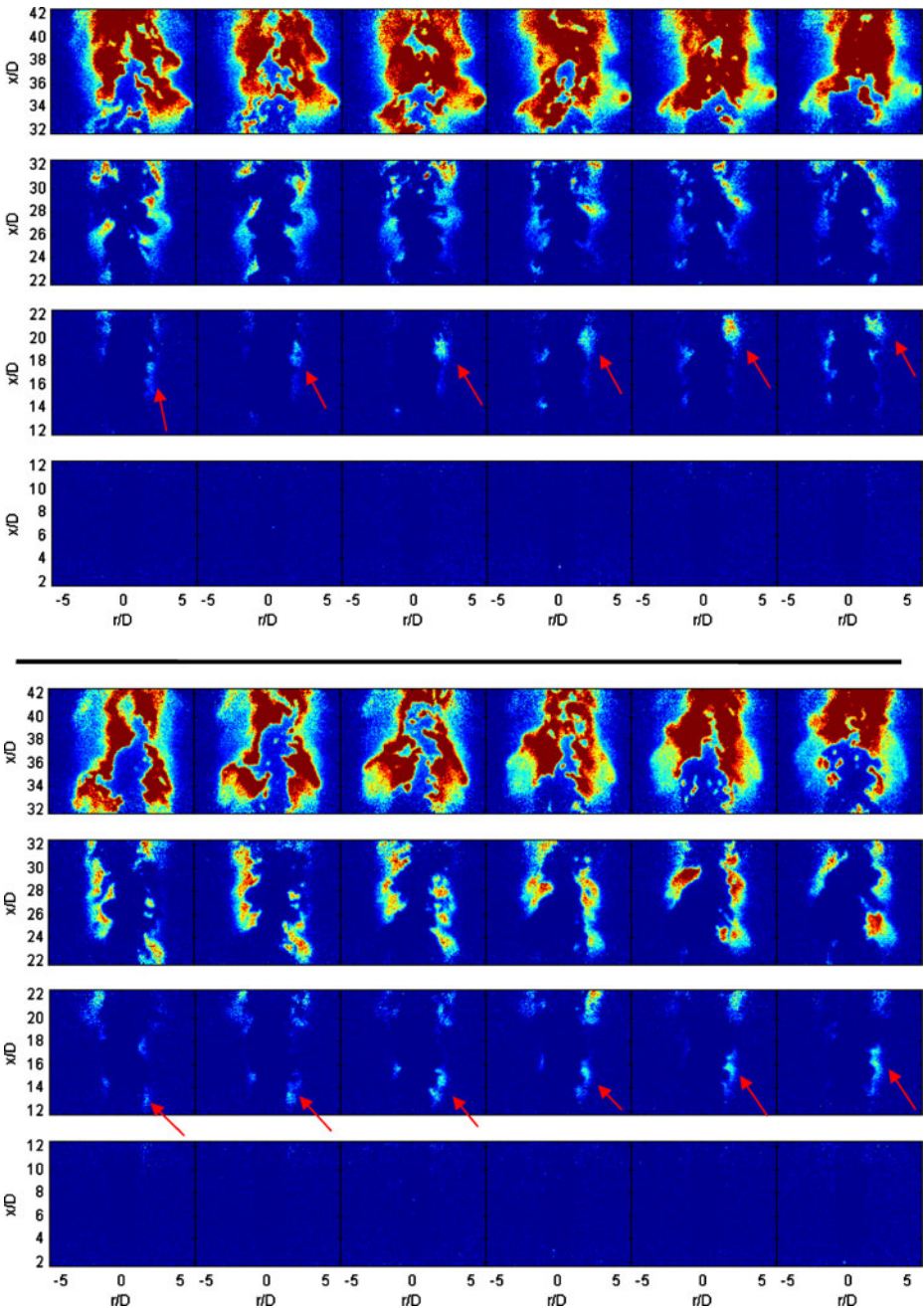
**Fig. 7** High Speed (5 kHz) imaging of OH-LIF in a methanol flame. The images are sequenced from left to right with a time spacing of 200 μs. The images start at x/D = 2 (*bottom*) in intervals of 10 D up to x/D = 42 (*top*). Image dimensions are 58 mm × 50 mm in physical space
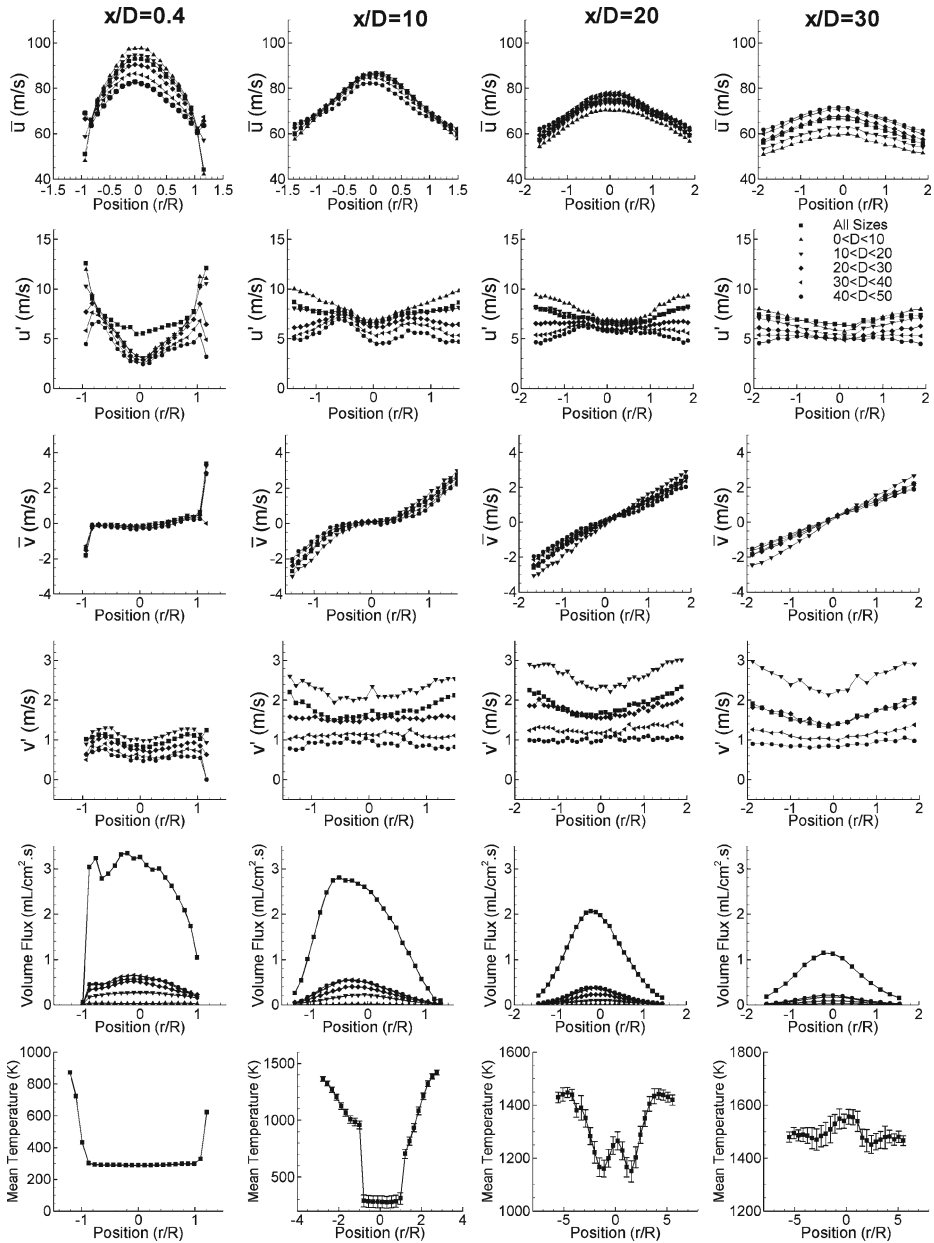
**Fig. 8** LDV/PDA and thermocouple measurements in Flame Mt2B taken at various axial locations from the exit plane (*left*) to x/D = 30 (*right*). The measurements are from top to bottom; axial mean velocity, axial rms velocity, radial mean velocity, radial rms velocity, axial volume flux and mean temperature. Droplet statistics are conditioned on droplet diameter. The smallest size bin (0 < d < 10 μm) is omitted in some cases due to lack of data in the bin

The trends measured in the mean axial velocities are expected in that the slip velocities for large droplets (taken with respect to the droplets smaller than 10 μm) are initially negative and then equilibrate around x/D = 10 before becoming positive at x/D = 20. For the droplet size range 40 < d < 50 μm, the mean slip velocity on the centerline changes from −16 m/s at x/D = 0.4 to 12 m/s at x/D = 30. The rms fluctuations in the axial velocity peak near the jet walls at the exit plane with values higher than 10 m/s measured for the smaller droplet sizes while those for the larger droplets (40 < d < 50 μm) peak around 6 m/s. Further downstream, the profiles of u' become gradually flatter where the separation between largest and smallest droplets decreases on the jet wings and increases on the centerline so that a difference of about 2 m/s is noted between the largest and smallest droplets size ranges shown here.

Profiles of the mean radial velocity, $\bar{v}$ show the expected symmetry around the centerline with measurements showing an increase to about 3 m/s at outer radial location with little variations with respect to droplet size and axial distance from the jet exit plane. The rms fluctuations in radial velocity, $v'$ exhibit flat profiles across the jet with the largest droplets having almost fixed values of $v' \sim 1$ m/s while smaller droplets in the size range 10 < d < 20 μm features higher radial dispersion with values of $v'$ around 3 m/s measured at x/D = 30. The lower radial dispersion for larger droplets is consistent with the expected higher Stokes numbers. The measured liquid volume fluxes show a significant decrease with axial distance and an increasing dominance of the large droplets. This is consistent with the fact that small droplets tend to evaporate first.

The measured mean temperature at the jet exit plane shows a uniform value of 288K which is lower than the ambient temperature due to evaporation of the methanol. At x/D = 10, the thermocouple was changed to the Platinum-Rhodium thermocouple described in Section 2.2. The centerline temperature here is measured as room temperature however this thermocouple cannot resolve small temperature difference at this low temperature. It is clear that, on the mean, there is no heat release in this region of the jet since the outer temperature increases only to the value of the co-flow (1430K). Further downstream at x/D = 20, the centerline mean temperature jumps to 1250K and then decreases slightly on either side. Referring to Fig. 3, this increase is in the region preceding the tip of the inner flame cone. At outer radial locations, the peak mean temperature increases to almost 1450K and the heat release on the centerline is noted by the additional increase in the mean centerline temperature at x/D = 30 (to a peak of 1550K) which corresponds to the tip of the inner flame cone.

## 4 Discussion

It is evident from the results presented here that there are features of similarities as well as differences between the auto-ignition of gaseous and spray fuels. The early formation of formaldehyde in the radical pool and the importance of kernels in initiating ignition (as illustrated in the images presented in Figs. 6 and 7) is a common phenomenon to both gaseous and liquid hydrocarbon fuels. An observed difference in spray flames with air carrier is the existence of an intensely reacting cone just downstream the initial ignition region which is characterized by very little heat release. This is also clear from the visual images of flames Mt2A, Mt2B and

Mt2C (Fig. 3) which show the intense luminosity at downstream locations of x/D = 30 − 40. This section provides some further insights into the nature of spray auto-ignition focusing on two specific aspects of flame structure, namely (i) the thickness of the evolving reaction zones as dictated by the width of the $HR_I$ profiles and (ii) the tendency of OH and $HR_I$ to approach the centerline at some downstream distance where significant heat release occurs.

Axial variations of the proximity of OH and $HR_I$ from the centerline and the widths of the $HR_I$ profiles are reported for the flames studied here in Figs. 10 and 11 respectively. The post processing required to obtain such information is now described aided by the diagrams presented in Fig. 9. The top half of Fig. 9 shows
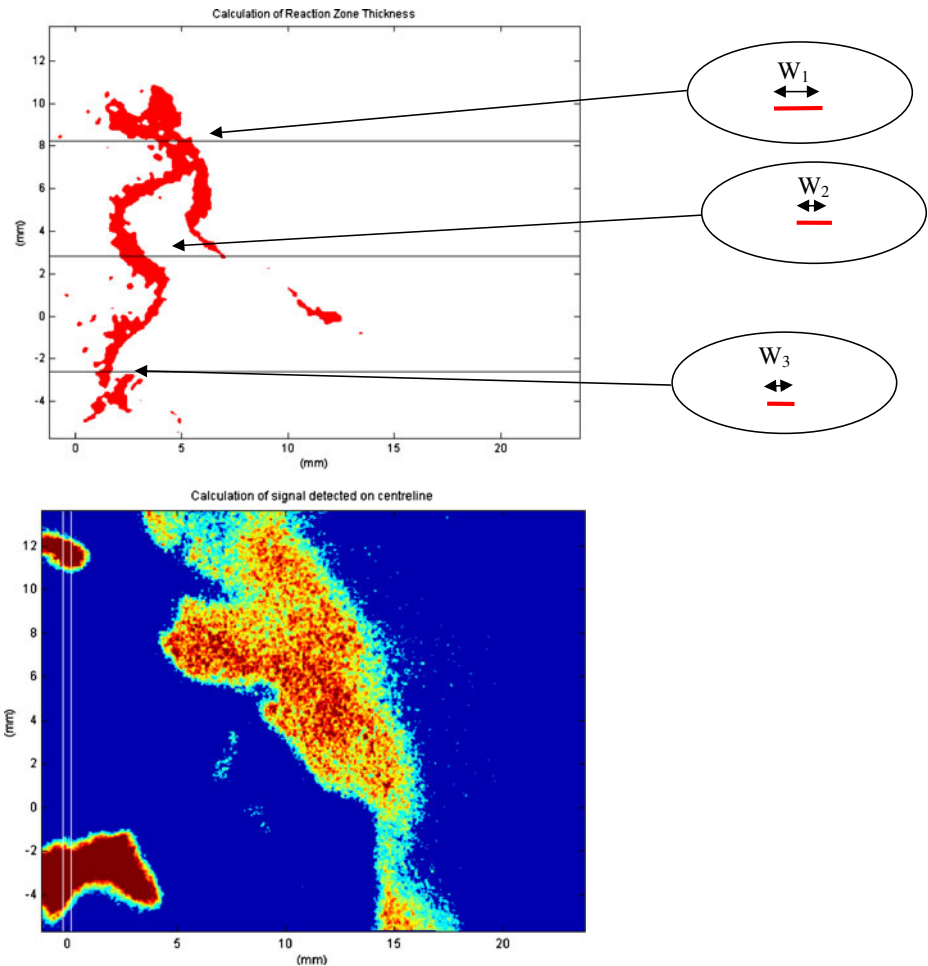


**Fig. 9** Diagram showing the calculation of the reaction zone thickness (*top*) and calculation of the signal detected on the centerline (*bottom*). The reaction zone thickness is calculated at three locations per image and measurements are averaged over 1000 images. The centerline signal is calculated by finding the percentage of pixels within the *vertical white lines* that contain a signal

the procedure for determining the reaction zone thickness. Taking an image of heat release as obtained from the product $[OH][CH_2O]$, three profiles are taken across the width of the image at the locations indicated by W1, W2 and W3 in the figure. The width of the reaction zone at these locations is recorded and stored. The process is repeated for 1000 images at each axial location and the average flame width is subsequently calculated. The bottom part of Fig. 9 shows the process for determining when OH and $HR_I$ signals are detected on the jet centerline. A strip, nine pixels wide is positioned on the centerline as indicated by the vertical lines in Fig. 9. In a given image, the percentage of pixels within this strip that are occupied by an OH signal or an $HR_I$ signal, is recorded. A coverage of 100% indicates that all of the pixels within this strip have detected a signal (of OH or $HR_I$, depending on the image being processed) while a 0% coverage indicates no detection. Again, 1000 images are used to obtain a good average at each axial location. The threshold number of counts required to be classified as a valid OH or $HR_I$ signal is 50 which is just a few counts above the background.

Figure 10 shows axial profiles of the percentage of pixels covered by OH and $HR_I$ on the centerline strip of six flames, namely Mt2A to C and Mt2AN to CN. For all flames shown on Fig. 10 and on the mean, there is neither OH nor heat release detected on the centerline for $x/D < 20$. Further downstream however, there is a tendency for both the OH and $HR_I$ to close in and increase on the centerline. It is evident from the profiles shown on the LHS of Fig. 10 (for the flame using air as carrier) that the percentage occupancy of both OH and $HR_I$ on the centerline increases from flames Mt2A, to Mt2B to Mt2C. In flame Mt2C, the mean centerline occupancy for OH reaches over 80% at $x/D = 40$ while that for $HR_I$ peaks around 30% at $x/D = 35$ and decreases further downstream.

It is notable that for the flames with nitrogen carrier (RHS of Fig. 10), the trends are similar to those using air as carrier but the rate of occupancy increase with axial distance is much slower. Additionally, the peak occupancy rate does not increase with increasing spray loading but stays somewhat constant peaking at $x/D = 40$ around 20% for OH and around 10% for $HR_I$ for all flames Mt2AN, Mt2BN and Mt2CN. The trends reported in Fig. 10 are consistent with the overall appearance of the flames in that with air carrier, premixing closer to the jet centerline is higher so as ignition kernels develop on the outer edges of the jet and travel downstream, these mixtures ignite and release heat as seen at $x/D{\sim}40$ in flames Mt2B and Mt2C (see Figs. 3 and 10). With nitrogen carrier, the mixing rates on the centerline do not change much within the 'valid cone' from flames Mt2AN to Mt2BN to Mt2CN so the presence of OH and heat release remains almost uniform.

Axial profiles of mean reaction zone thicknesses are shown in Fig. 11 for the six flames studied here and for axial distance ranging from $x/D = 25$ to 40. Even though the general trend in all cases is for the reaction zone width to increase with increasing axial distance, such increases are minimal for the flames with nitrogen carrier and range from 0.4 to 0.6 mm for the three flames (Mt2AN to Mt2BN to Mt2CN). Conversely, and with air as spray carrier, the width of the reaction zones at $x/D = 40$ increases from about 0.6 mm to 1.0 mm and to 1.2 mm for flames, Mt2A, Mt2B, and Mt2C, respectively. These trends are consistent with the fact that with air as carrier, the flame endures a higher degree of partial premixing and hence spatial broadening of reaction zones. With nitrogen as carrier, however, the flame maintains a diffusion-like structure and hence a uniform reaction zone width.
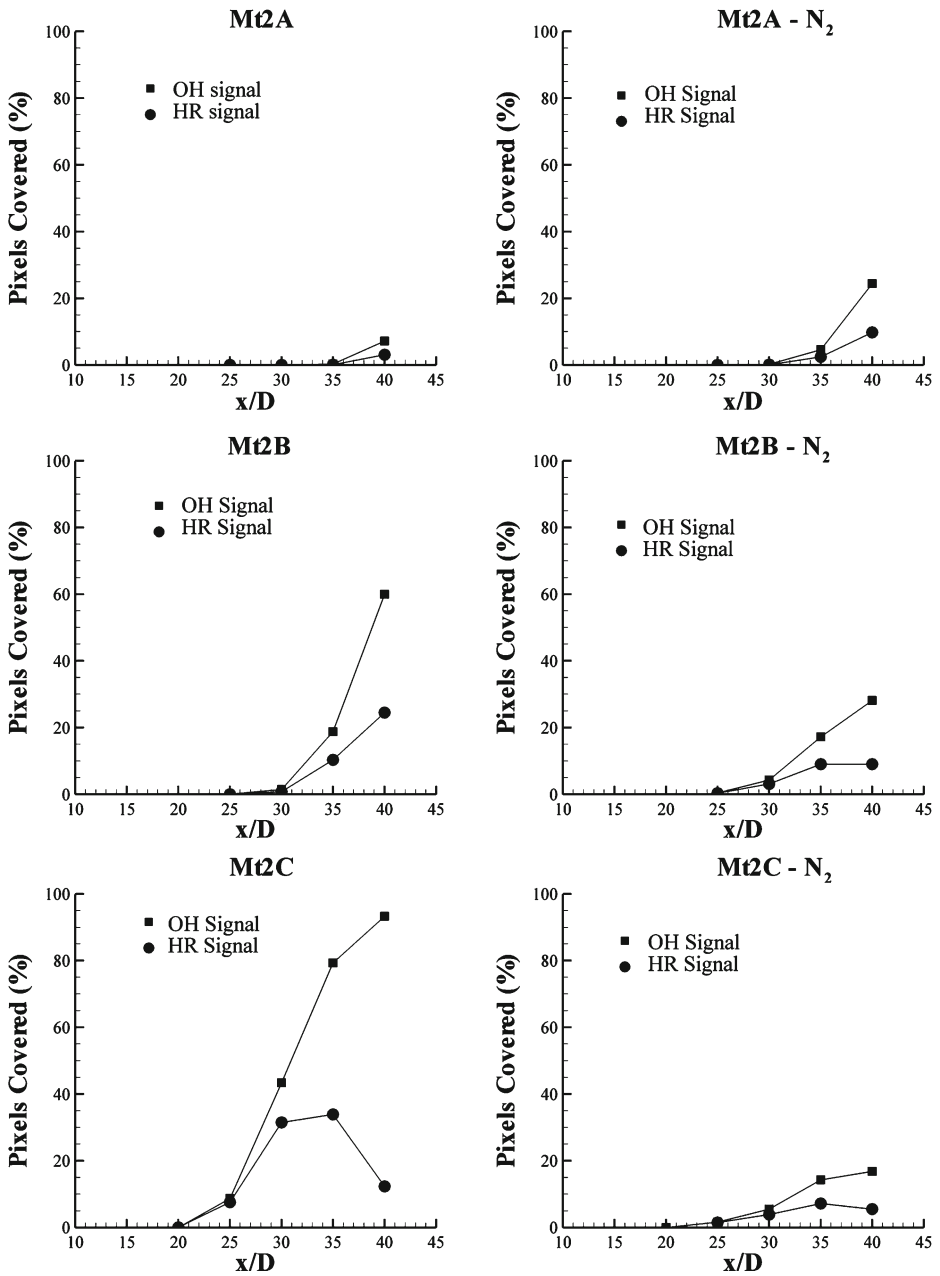
**Fig. 10** Plots showing the relative amount of OH and $HR_I$ present on the centerline for six different methanol flames

**Fig. 11** Plots of reaction zone thickness for three flames, Mt2A/Mt2AN, Mt2B/Mt2BN and Mt2C/Mt2CN
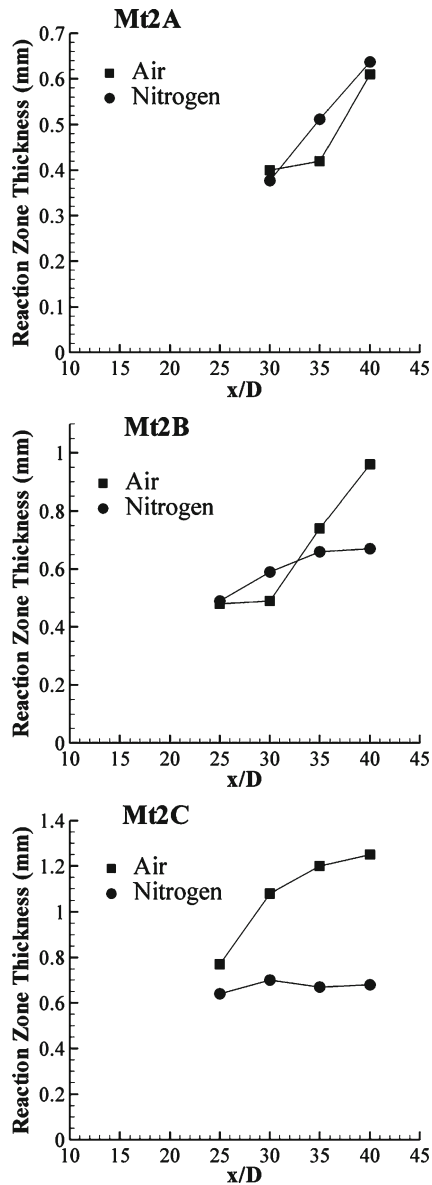


## 5 Conclusions

High-speed (5 kHz) LIF-OH imaging is performed here to obtain qualitative, time-resolved sequences of the evolution of the auto-ignition process in turbulent, dilute spray flames issuing in a hot co-flow. Additionally, joint imaging of LIF-OH-CH$_2$O albeit at a low repetition rate of 10 Hz, yields qualitative information about regions of heat release given by the product [OH][CH$_2$O].

Aspects of similarities as well as differences are found between the auto-ignition of gaseous fuels and those of dilute sprays. A common feature is that formaldehyde is detected earlier than OH implying that the former is a key precursor in the initiation of auto-ignition. Kernels of OH that grow to ignite the main flame are detected although these occur off the centreline of the jet. Breakages and closures in the OH profiles are detected as is commonly found for gaseous flames. The following differences are noted:

- Double reaction zones are detected frequently and this may be due to vaporizing droplets leading to mixing and the local formation of ignitable mixtures.
- When air is used as spray carrier, reaction zones broaden with distance, possibly due to increased partial premixing and regions of intense heat release occur near the flame centreline further downstream. In addition, OH fields start on the edges of the jet before closing into the centreline at downstream locations.
- With nitrogen as carrier, the flame maintains a nominal diffusion-like structure with reaction zones of uniform width and substantially less concentration of heat release on the flame centreline.

# References

1. O'Loughlin, W., Masri, A.R.: A new burner for studying auto-ignition in turbulent dilute sprays. Combust. Flame **158**(8), 1577–1590 (2011)
2. Gordon, R.L., Masri, A.R., Mastorakos, E.: Simultaneous Rayleigh temperature, OH- and $CH_2O$-LIF imaging of methane jets in a vitiated coflow. Combust. Flame **155**, 181–195 (2008)
3. Cabra, R., Chen, J.-Y., Dibble, R.W., Karpetis, A.N.: Lifted methane-air jet flames in a vitiated coflow. Combust. Flame **143**, 491–506 (2005)
4. Cabra, R., Hamano, Y., Chen, J.Y., Dibble, R.W., Acosta, F., Holve, D.: Ensemble diffraction measurements of spray combustion in a novel vitiated co-flow turbulent jet flame burner. NASA Report:NASA/CR—2000-210466 (2000)
5. Cabra, R., Dibble, R.W., Chen, J.Y.: Characterization of liquid fuel evaporation of a lifted methanol spray flame in a vitiated co-flow burner. NASA Report:NASA/CR—2002-212083 (2002)
6. Markides, C.N., Mastorakos, E.: An experimental study of hydrogen autoignition in a turbulent co-flow of heated air. Proc. Combust. Inst. **30**, 883–891 (2005)
7. Duwig, C., Fuchs, L.: Large eddy simulation of a $H_2/N_2$ lifted flame in a vitiated co-flow. Combust. Sci. Technol. **180**(3), 453–480 (2008)
8. Hilbert, R., Thevenin, D.: Autoignition of turbulent non-premixed flames investigated using direct numerical simulations. Combust. Flame **128**(1—2), 22–37 (2002)
9. Mastorakos, E., Baritaud, T.B., Poinsot, T.J.: Numerical simulations of autoignition in turbulent mixing flows. Combust. Flame **109**(1–2), 198–223 (1997)
10. Im, H.G., Chen, J.H., Law, C.K.: Ignition of hydrogen-air mixing layer in turbulent flows. Proc. Combust. Inst. **27**, 1047–1056 (1998)
11. Sreedhara, S., Lakshmisha, K.N.: Autoignition in a non-premixed medium: DNS studies on the effects of three-dimensional turbulence. Proc. Combust. Inst. 29, 2051-2059 (2002)
12. Domingo, P., Vervisch, L.: Triple flames and partially premixed combustion in autoignition of non-premixed turbulent mixtures. Proc. Combust. Inst. **26**, 233–240 (1996)
13. Mastorakos, E., Bilger, R.W.: Second-order conditional moment closure for the autoignition of turbulent flows. Phys. Fluids **10**(6), 1246–1248 (1998)
14. Echekki, T., Chen, J.H.: Direct numerical simulation of autoignition in non-homogeneous hydrogen-air mixtures. Combust. Flame **134**, 169–191 (2003)

15. Echekki, T., Chen, J.H.: High-temperature combustion in autoigniting non-homogeneous hydrogen/air mixtures. Proc. Combust. Inst.**29**, 2061–2068 (2002)
16. Wright, Y.M., Margari, O.-N., Boulouchos, K., Paola, G.D., Mastorakos, E.: Experiments and simulations of n-heptane spray auto-ignition in a closed combustion chamber at diesel engine conditions. Flow Turbul. Combust. **84**, 49–78 (2010)
17. Vogel, S., Hasse, C., Gronki, J., Andersson, S., Peters, N., Wolfrum, J., Schulz, C.: Numerical simulation and laser-based imaging of mixture formation, ignition, and soot formation in a diesel spray. Proc. Combust. Inst. **30**, 2029–2036 (2005)
18. Zhu, M., Bray, K.N.C., Rogg, B.: PDF modelling of spray autoignition in high pressure turbulent flows. Combust. Sci. Technol. **120**, 357–379 (1996)
19. Durand, P., Gorokhovski, M., Borghi, R.: An application of the probability density function model to diesel engine combustion. Combust. Sci. Technol. **144**(1–6), 47–78 (1999)
20. Boileau, M., Pascaud, S., Riber, E., Cuenot, B., Gicquel, L.Y.M., Poinsot, T.J., Cazalens, M.: Investigation of two-fluid methods for large eddy simulation of spray combustion in gas turbines. Flow Turbul. Combust. **80**, 291–321 (2008)
21. Boileau, M., Staffelbach, G., Cuenot, B., Poinsot, T., Berat, C.: LES of an ignition sequence in a gas turbine engine. Combust. Flame **154**, 2–22 (2008)
22. Kim, S.H., Huh, K.Y., Fraser, R.A.: Modeling autoignition of a turbulent methane jet by the conditional moment closure model. Proc. Combust. Inst. **28**, 185–191 (2000)
23. Kim, W.T., Huh, K.Y.: Numerical simulation of spray autoignition by the first order conditional moment closure model. Proc. Combust. Inst. **29**, 569–576 (2002)
24. Wright, Y.M., Paola, G.D., Boulouchos, K., Mastorakos, E.: Simulations of spray autoignition and flame establishment with two-dimensional CMC. Combust. Flame **143**, 402–419 (2005)
25. Schroll, P., Wandel, A.P., Cant, R.S., Mastorakos, E.: Direct numerical simulations of autoignition in turbulent two-phase flows. Proc. Combust. Inst. **32**, 2275–2282 (2009)
26. Seo, J., Huh, K.Y.: Analysis of combustion regimes and conditional statistics of autoigniting turbulent n-heptane sprays. Proc. Combust. Inst. **33**, 2127–2134 (2011)
27. Wang, Y., Rutland, C.J.: Direct numerical simulation of ignition in turbulent n-heptane liquid-fuel spray jets. Combust. Flame **149**(4), 353–365 (2007)
28. Paul, P.H., Najm, H.N.: Planar laser-induced fluorescence imaging of flame heat release rate. Proc. Combust. Inst. **27**, 43–50 (1998)
29. Bockle, S., Kazenwadel, J., Kunzelmann, T., Shin, D.-I., Schultz, C., Wolfrum, J.: Simultaneous single-shot laser-based imaging of formaldehyde, OH and temperature in turbulent flames. Proc. Combust. Inst. **28**, 279–286 (2000)
30. Fayoux, A., Zahringer, K., Gicquel, O., Rolon, J.C.: Experimental and numerical determination of heat release in counterflow premixed laminar flames. Proc. Combust. Inst. **30**, 251–257 (2005)
31. Gounder, J.D.: An Experimental Investigation of Non-reacting and Reacting Spray Jets. The University of Sydney (2009)
32. Dally, B.B., Karpetis, A.N., Barlow, R.S.: Structure of turbulent non-premixed jet flames in a diluted hot coflow. Proc. Combust. Inst. **29**, 1147–1154 (2002)
33. Medwell, P.R., Kalt, P.A.M., Dally, B.B.: Imaging of diluted turbulent ethylene flames stabilized on a Jet in Hot Coflow (JHC) burner. Combust. Flame **152**, 100–113 (2008)
34. Medwell, P.R., Kalt, P.A.M., Dally, B.B.: Reaction zone weakening effects under hot and diluted oxidant stream conditions. Combust. Sci. Technol. **181**, 937–953 (2009)
35. Gordon, R.L., Masri, A.R., Mastorakos, E.: Heat release rate as represented by [OH]x[CH$_2$O] and its role in autoignition. Combust. Theory Model. **13**(4), 645–670 (2009)
36. Paola, G.D., Mastorakos, E., Wright, Y.M., Boulouchos, K.: Diesel engine simulations with multi-dimensional conditional moment closure. Combust. Sci. Technol. **180**, 883–899 (2008)
37. Lindstedt, R.P., Meyer, M.P.: A dimensionally reduced reaction mechanism for methanol oxidation. Proc. Combust. Inst. **29**, 1395–1402 (2002)
38. Juddoo, M., Masri, A.R.: High-speed OH-PLIF imaging of extinction and re-ignition in non-premixed flames with various levels of oxygenation. Combust. Flame **158**(5), 902–914 (2011)